Microbially-mediated formation of Ca-Fe carbonates during dissimilatory ferrihydrite reduction: Implications for the origin of sedimentary ankerite

Deng Liu[1, 2, *], Jinpeng Cao[2], Shanshan Yang[2], Yating Yin[2], Pengcong Wang[1], Dominic Papineau[1, 3, 4, 5], Hongmei Wang[1, 2], Xuan Qiu[1], Genming Luo[1], Zongmin Zhu[1], and Fengping Wang[6]

[1]State Key Laboratory of Biogeology and Environmental Geology, China University of Geosciences, Wuhan 430074, China

[2]School of Environmental Studies, China University of Geosciences, Wuhan 430074, China

[3]London Centre for Nanotechnology, University College London, 17-19 Gordon Street, London, UK

[4]Department of Earth Sciences, University College London, London, UK

[5]Center for Planetary Sciences, University College London and Birkbeck College London, London, UK

[6]State Key Laboratory of Microbial Metabolism, State Key Laboratory of Ocean Engineering, Shanghai Jiao Tong University, Shanghai 200240, China

Corresponding author: Deng Liu (liudeng@cug.edu.cn)

Revised for *Science China Earth Sciences*

March 19, 2023

Abstract

The origin of sedimentary dolomite has become a long-standing problem in the Earth Sciences. Some carbonate minerals like ankerite have the same crystal structure as dolomite, hence their genesis may provide clues to help solving the dolomite problem. The purpose of this study was to probe whether microbial activity can be involved in the formation of ankerite. Bio-carbonation experiments associated with microbial iron reduction were performed in batch systems with various concentrations of Ca^{2+} (0-20 mM), with a marine iron-reducing bacterium *Shewanella piezotolerans* WP3 as the reaction mediator, and with lactate and ferrihydrite as the respective electron donor and acceptor. Our biomineralization data showed that Ca-amendments expedited microbially-mediated ferrihydrite reduction by enhancing the adhesion between WP3 cells and ferrihydrite particles. After bioreduction, siderite occurred as the principal secondary mineral in the Ca-free systems. Instead, Ca-Fe carbonates were formed when Ca^{2+} ions were present. The $CaCO_3$ content of microbially-induced Ca-Fe carbonates was positively correlated with the initial Ca^{2+} concentration. The Ca-Fe carbonate phase produced in the 20 mM Ca-amended biosystems had a chemical formula of $Ca_{0.8}Fe_{1.2}(CO_3)_2$, which is close to the theoretical composition of ankerite. This ankerite-like phase was nanometric in size and spherical, Ca-Fe disordered, and structurally defective. Our simulated diagenesis experiments further demonstrated that the resulting ankerite-like phase could be converted into ordered ankerite under hydrothermal conditions. We introduced the term “proto-ankerite” to define the Ca-Fe phases that possess near-ankerite stoichiometry but disordered cation arrangement. On

the basis of the present study, we proposed herein that microbial activity is an important contributor to the genesis of sedimentary ankerite by providing the metastable Ca-Fe carbonate precursors.

Keywords: Ankerite; Proto-ankerite; Microbial iron reduction; Dolomite problem; Mineral transformation

1. Introduction

Crystalline calcium-bearing carbonates are important components of sediments and sedimentary rocks. These carbonate minerals have been documented as an archive of recent and past Earth's chemical and climatic changes (Higgins et al., 2018; Chang et al., 2020). Furthermore, they represent typical skeletal constituents of marine invertebrates (Marin et al., 1996), and are profoundly involved in the whole-Earth carbon cycle (Schrag et al., 2013; Liu et al., 2019). Despite the importance of these carbonates, their formation mechanism and kinetics are not well understood. Dolomite [$CaMg(CO_3)_2$], in particular, has been an enigmatic mineral for over two centuries. The long-lasting debate about the origin of dolomite, known as the "dolomite problem", is mainly due to the apparent mismatch between the difficulty of dolomite synthesis under ambient conditions and its widespread occurrence in sedimentary rocks (Gregg et al., 2015; Guo et al., 2017; Petrash et al., 2017).

In nature, some double carbonates such as ankerite [$CaFe(CO_3)_2$], kutnahorite [$CaMn(CO_3)_2$], and minrecordite [$CaZn(CO_3)_2$] also have the trigonal and rhombohedral structure of dolomite, and hence they are defined as dolomite group

minerals (Pimentel and Pina, 2016). These double carbonates have received growing attention because insights into the formation mechanism of these minerals would provide clues to better understand the genesis of sedimentary dolomite (Liu and Li, 2020).

Ankerite is the second most common dolomite group mineral after dolomite (Gregg et al., 2015). Noticeably, "hypothetical" ankerite that has the chemical composition of $CaFe(CO_3)_2$ and Ca-Fe ordering is not found to occur naturally (Gregg et al., 2015). According to the International Mineralogical Association (IMA) guidelines, natural ankerite is a $Ca(Mg, Fe)(CO_3)_2$ carbonate, in which more than 50 mol% Mg^{2+} ions in the dolomitic structure are substituted by Fe^{2+} ions (Gregg et al., 2015; Xu et al., 2019). Similar to dolomite, ankerite does not easily precipitate from saturated solutions at Earth surface temperatures (Gregg et al., 2015; Xu et al., 2019). Therefore, sedimentary ankerite has often been proposed as a diagenetic mineral replacing calcite, for instance through the following reaction (Hendry et al., 2000):

$$4CaCO_3\,(\text{calcite}) + Fe^{2+} + Mg^{2+} \rightarrow 2CaMg_{0.5}Fe_{0.5}(CO_3)_2\,(\text{ankerite}) + 2Ca^{2+}$$

Such replacement reaction is usually thought to require temperatures between 100 and 200 °C during deep burial (e.g., Hendry et al., 2000).

Microorganisms are cosmopolitan on Earth and they show potential to mediate the precipitation and crystallization of various minerals (Xie et al., 2016). Of particular note, considerable research, mostly based on laboratory simulation experiments, has shown that some types of microbes can overcome the magnesium-hydration barrier and catalyze the precipitation of dolomite or other Mg-Ca carbonates under low-

temperature conditions (Petrash et al., 2017, and references therein). In most reports, however, microbially-induced dolomite has disordered cations and is often described as disordered proto-dolomite or very high-Mg calcite (Gregg et al., 2015). It has been suggested that low-temperature proto-dolomite can convert into their ordered counterparts during burial diagenesis and/or metamorphism (Zhang et al., 2012; Zheng et al., 2021). This emerging microbial model of dolomite formation has been applied to interpret the origin of some sedimentary dolomites (Perri and Tucker, 2007; You et al., 2014; Wen et al., 2020; Li et al., 2021). Since ankerite belongs to the dolomite group, it has been hypothesized that microorganisms might be a triggering factor for the formation of ankerite (e.g., Xu et al., 2019). Hence, laboratory experiments are needed to test this hypothesis.

In the present study, we performed cultivation experiments to test whether dissimilatory iron-reducing bacteria (DIRB) can enhance the incorporation of Ca^{2+} into Ca-Fe carbonate precipitates upon the biological reduction of ferrihydrite, which is the most common iron hydroxide found in sedimentary environments. Specifically, the Ca-Fe carbonate formed in such biological systems with high Ca/Fe ratio tested herein had a stoichiometry close to the "theoretical" ankerite [$CaFe(CO_3)_2$], but was mostly cation disordered. We thus suggest the term of "proto-ankerite" to describe this phase since it could serve as a metastable precursor for ordered ankerite, as subsequently demonstrated in our hydrothermal experiments. Our experiments provide an alternative explanation for the origin of sedimentary ankerite, that is, low-temperature Ca-Fe carbonate precursors (e.g., proto-ankerite) are primarily stimulated by microbial

activity and subsequently converted into more stable ankerite through a diagenesis-controlled recrystallization reaction.

2. Materials and methods

2.1. Bacterial strain and culture medium

The *Shewanella* strains are known for their dissimilatory Fe(III)-respiring capabilities, and they represent the most abundant *Proteobacteria* in ferruginous seafloor environments (Wang et al., 2008). *Shewanella piezotolerans* WP3, a marine facultative DIRB originally isolated from West Pacific sediments (Wang et al., 2008), was selected for this study. Cells of strain WP3 were first cultured aerobically in marine medium 2216E (with 5 g/L peptone, 1 g/L yeast extract, 0.01 g $FePO_4$, 34 g/L NaCl, pH=7.5) at 20 °C with constant agitation (160 rpm). Once cell growth reached the mid to late log phase (as indicated by measurements of OD_{600}), WP3 cells were harvested in an anaerobic chamber (filled with 98% N_2 and 2% H_2, Coy Laboratory Products, USA) by centrifugation (8000 ×g, 10 min) and resuspended in pre-deoxygenated marine salt bicarbonate buffer (2.5 g/L $NaHCO_3$, 30 g/L NaCl, 10 g/L $MgCl_2 \cdot 6H_2O$, 1 g/L KCl and 1 g/L $CaCl_2$, pH=7.5). The harvested cells were kept in serum bottles in the dark at 4 °C for future use.

2.2. Preparation of ferrihydrite

Ferrihydrite was prepared based on the method of Schwertmann and Cornell (1991). In brief, a 5 M KOH solution was added slowly into a 1 M $Fe(NO_3)_3 \cdot 9H_2O$ with vigorous stirring to the pH 7-8. The mixture was allowed to stand for 3 hours at room

temperature. The ferrihydrite precipitates were collected by centrifugation (8000 ×g, 15 min), repeatedly washed with double distilled water, and made into slurry to obtain a Fe(III) concentration of 0.3 M. This slurry served as a stock solution for subsequent iron reduction experiments.

2.3. Microbial iron reduction and adhesion experiments

Batch experiments were conducted with various concentrations of Ca^{2+} to evaluate whether Ca^{2+} could be incorporated into mineral precipitates during microbial reduction of ferrihydrite. A modified basal medium for *Shewanella* species was used for microbial reduction experiments (Roden et al., 2002). The composition of the medium consisted of 30 mM $NaHCO_3$, 50 mM $MgCl_2$, 0.5 mM KH_2PO_4, 513 mM NaCl, different concentrations of $CaCl_2$ (0, 5, 10 and 20 mM), 0.2 g/L yeast extract, 1 mL trace elements (Roden et al., 2002), and 1 mL vitamin solution (Roden et al., 2002). The medium pH was adjusted to 7.5 by adding 0.1 M NaOH as needed. The modified basal medium was purged with ultra-pure N_2 and transferred into the anaerobic chamber for membrane filtration (MF, Millipore, USA; pore size of 0.22 μm). This filtered medium was dispensed into sterile serum bottles and sealed with butyl rubber stoppers. The serum bottles were supplemented with ferrihydrite stock solution as the sole electron acceptor (10 mM, final concentration) and pre-filtered sterilized sodium lactate as the electron donor (final concentration of 20 mM). An aliquot of WP3 suspension was then injected into selected bottles to achieve a final concentration of about 1×10^7 cells/mL. In addition, abiotic controls without bacterial inoculum were also performed. Both biotic and abiotic reactors were conducted in duplicate. The experimental bottles were

156 wrapped in aluminum foil to block light and then placed in an incubator at 20 °C
157 without agitation.

158 Microbial adhesion to the Fe(III) minerals is a crucial step in microbial iron
159 reduction. To examine the influence of Ca^{2+} on microbial reduction of ferrihydrite, the
160 adhesion experiments were performed in the aforementioned basal medium in which
161 the organic substrates were omitted. The adhesion capacity of WP3 to ferrihydrite was
162 determined by the methods described previously (Zhao et al., 2014). In brief, pre-
163 washed WP3 cells were added into 30 mM ferrihydrite suspensions to obtain a cell
164 density of about 1×10^7 cells/mL. The initial concentration of Ca^{2+} was varied in the
165 range of 0-20 mM. The cell-mineral mixtures were agitated at 150 rpm at 20 °C. After
166 a one hour-incubation period, the un-adhered cells of strain WP3 were separated from
167 the attached cells and ferrihydrite particles by injecting 60% sucrose solution (w/w).
168 These sucrose-amended suspensions were centrifuged at 8000 ×g for 10 min. The
169 numbers of un-adhered cells in the supernatants were determined with acridine-orange
170 direct count (AODC) by epifluorescence microscopy (Olympus BX50, Olympus
171 Optical Co., Tokyo, Japan).

172 **2.4. Hydrothermal alteration experiments**

173 Our experiments demonstrated that strain WP3 was able to trigger the formation
174 of Ca-Fe carbonates accompanied by the bioreduction of ferrihydrite (see later Section
175 3.3 for details). We hypothesized that Ca-Fe carbonate neoformations (especially proto-
176 ankerite) could transform into ankerite during burial diagenesis. In order to test such
177 hypothesis, hydrothermal simulation experiments were further carried out to mimic the

178 fluid-induced mineral transformation.

179 Proto-ankerite that was produced in the bioreactors with 20 mM Ca^{2+} was selected
180 as a representative Ca-Fe carbonate for hydrothermal experiments. In a typical
181 experimental run, 500 mg of proto-ankerite powder and 25 mL anaerobic marine salt
182 bicarbonate buffer (2.5 g/L $NaHCO_3$, 30 g/L NaCl, 10 g/L $MgCl_2 \cdot 6H_2O$, 1 g/L KCl and
183 1 g/L $CaCl_2$, pH=7.5) were loaded in a sealed Teflon-lined bomb and heated up to
184 100 °C for two months, and then cooled to room temperature. The reaction solids were
185 separated by centrifugation at 8000 ×g for 10 min. The resulting pellet was further
186 washed with pre-deoxygenated double distilled water three times and dried in the
187 anaerobic chamber.

188 **2.5. Analyses**

189 **2.5.1. Wet chemistry**

190 At each sampling point, solution pH was determined in the supernatants using a
191 Hach multimeter (Hach Co., USA). Cell density was estimated as colony forming units
192 (CFUs). The concentrations of NH_4^+ and solution alkalinity were determined
193 spectrophotometrically as described by McLeod (1992) and Sarazin et al. (1999),
194 respectively. Briefly, two mL aliquots of cell-ferrihydrite suspension were sampled at
195 selected time points with a sterile and anoxic syringe followed by centrifugation at 8000
196 ×g for 10 minutes. For NH_4^+ measurement, 1 mL of the supernatant was mixed with 0.5
197 mL of sodium salicylate-sodium hydroxide solution and 0.2 mL of sodium
198 dichloroisocyanurate solution. The mixture was measured with a UV-
199 spectrophotometer (Shimadzu UV-1800, Shimadzu, Japan) at 660 nm after 30 min of

reaction time. Specifically for alkalinity determination, another 1 mL of supernatant was added into an equal volume of colored reagent that consists of 0.01 M formic acid and 0.05 g/L Bromophenol-Blue. Absorbances were measured at 590 nm with $NaHCO_3$ as a standard.

The concentrations of total Fe(II) and aqueous Fe(II) were analyzed by the ferrozine method (Stookey, 1970). Specifically for total Fe(II), 0.5 mL mineral slurry was withdrawn by syringe and injected into 0.5 mL of 1 N HCl. After 24 h incubation in the dark, a 0.1-mL sample of the extract was added to1 mL of ferrozine (1 g/L) in 50 mM HEPES buffer. The absorbance at 562 nm was determined and compared to Fe(II) standards of ferrous ethylene diammonium sulfate. Aqueous Fe(II) concentration was measured after filtering the mineral slurry through a syringe membrane filter (0.22 μm). Samples of Ca^{2+} and Mg^{2+} ions were collected from the supernatants following centrifugation (8000 ×g15 min) and their concentrations were measured with inductively coupled plasma-optical emission spectrometry (ICP-OES, Thermofisher ICAP6300, USA).

2.5.2. Mineral characterization

The zeta potential (ξ) of ferrihydrite suspension in the uninoculated medium as function of different concentrations of Ca^{2+} was measured using a Zeta potential analyzer (ZetaSizer Nano ZS, Malvern Instruments, UK). The bioreduced samples were characterized by X-ray diffraction (XRD), Mössbauer spectroscopy, and scanning and transmission electron microscopy (SEM and TEM). Prior to XRD measurements, samples were washed with pre-deoxygenated water three times to remove residual salts

and dried at 20 °C in an anaerobic chamber. The mineral powders were X-rayed from 10 to 60º 2θ using a Bruker D8 Advance XRD (Bruker, Germany) with Cu Kα radiation at 40 kV and 40 mA. The XRD data were analyzed with JADE 6.0 software (MDI, Livermore, USA) to identify phase. The elemental distribution of solid phases was also studied by ICP-OES after digestion with HNO_3 (trace metal grade). The morphology and chemical composition of biogenic minerals before and after hydrothermal treatments were examined using a Hitachi SU8010 SEM (Hitachi, Japan), which is equipped with an energy dispersive X-ray spectroscopy (EDS) detector (Oxford Instruments XMax 80, UK). The samples for SEM observation were Pt-coated prior to analysis. Then, samples were prepared for TEM analysis by dispersing the mineral powders in ethanol under ultra-sonication and depositing the product on carbon-coated 300 mesh copper grids. TEM observations were performed using a JEOL JEM-2100F (JEOL, Japan) with a LaB_6 source, operating at 200 kV. The observations were carried out in the modes of bright field imaging and selected area electron diffraction (SAED). Crystallographic analysis of TEM images was performed using DigitalMicrograph software (Gatan Inc., USA).

3. Results

3.1. Changes in wet chemistry during microbial iron reduction

During the incubation period, the pH in the bioreactors steadily increased within the first 15 days and then leveled off with time (Figure 1a). At the end of experiments (50 days), the pH rose from an initial value of ca. 7.50 to 8.36, 8.21, 7.90 and 8.04 in

244 the biosystems with 0, 5, 10 and 20 mM Ca^{2+}, respectively. The pH in the abiotic
245 reactors increased slightly to 7.74 after 50 days. There were no CFUs observed in the
246 abiotic controls. In contrast, the cell density in the bioreactors exhibited a rapid rise for
247 the first 7 or 10 days but a gradual decline afterwards (Figure 1b). Whereas insignificant
248 NH_4^+ was produced in abiotic controls, the concentrations of NH_4^+ of the bioreduction
249 experiments quickly increased within the first 7 days followed by a slower increase and
250 a final plateau (around 5 mM) (Figure 1c), which indicates that microbial
251 ammonification took place in the incubation systems. Furthermore, the increase of
252 solution alkalinity was also observed in the bioreactors (Figure 1d).

253 As illustrated in Figure 2a, significant accumulation of total Fe(II) was detected
254 when ferrihydrite was exposed to *S. piezotolerans* WP3, consistent with a previous
255 study (Wu et al., 2011). Unlike the biotic experiments, a negligible change in the
256 concentration of total Fe(II) in abiotic control experiments was observed. Moreover, it
257 was noted that the presence of Ca led to higher rates of microbial iron reduction within
258 the first 20 days. However, nearly similar reduction rates were observed among the Ca-
259 containing biosystems, regardless of the amount of Ca used. A two-stage increasing
260 trend was found in these biosystems: a rapid increase for the initial incubation period,
261 followed by a moderate increase for the subsequent incubation period (Figure 2a).
262 Although different initial bioreduction rates occurred with and without Ca^{2+} ions, the
263 final extents of ferrihydrite reduction were comparable at 76.4%, 77.7%, 83.5% and
264 80.0% for the bioreactors with 0, 5, 10 and 20 mM Ca^{2+}, respectively. The
265 concentrations of aqueous Fe(II) in all biotic treatments increased in the initial

incubation period (30 days for Ca-free systems and 15 or 20 days for Ca-amended reactors) (Figure 2b). Subsequent to these increases, aqueous Fe(II) was gradually removed from solutions in all biotic experiments. Aqueous Mg and Ca were also measured to assess their fate during microbial reduction of ferrihydrite (Figure 2c and d). In general, during the 50-day incubation experiments, the concentrations of Mg^{2+} remained unchanged in all biological reduction experiments (Figure 2c). In contrast, a decline in Ca^{2+} ions was observed during microbial iron reduction (Figure 2d). At the end of the experiments, the removal percentages of Ca during microbial iron reduction were estimated as 31.3%, 33.0% and 23.8% for the biosystems with 5, 10, and 20 mM Ca^{2+}, respectively.

3.2. Zeta potential of ferrihydrite and bacterial adhesion in the presence of Ca^{2+}

The zeta potential measurements showed that calcium ions had a significant impact on the surface electronic property of ferrihydrite particles (Figure 3). In the absence of Ca^{2+}, the ferrihydrite surface carried a slight negative charge (as indicated by the ξ values ranging from -18.2 to -13.8 mV) at pH 7-9. When Ca^{2+} ions were introduced into the mineral suspensions, the ξ values became positive and they increased with the increasing concentration of Ca^{2+} (Figure 3).

In the absence of Ca^{2+}, the percentage of WP3 cells attached to ferrihydrite particles was ca. 84% in one hour. Within the Ca-amended systems, the percent adhesion significantly increased to around 97%, regardless Ca^{2+} concentration.

3.3. Mineralogical, chemical and morphological analyses of solid products after bioreduction

3.3.1. XRD and ICP-OES

As shown in Figure 4, XRD patterns of the bioreduced products exhibited reflections of (012), (104), (110), (113), (202), (018) and (116) planes, which indicate the presence of the hexagonal (rhombohedral) structure. Specifically, the diffraction peaks of solid phases from the Ca-free biosystems matched well with those of siderite standard (PDF#29-0696) (Figure 4a), thus demonstrating that siderite was the major phase in these experiments. More interestingly, the XRD peaks of the solid products significantly shifted to lower 2θ values with increasing concentrations of Ca^{2+}, indicating the formation of Ca-Fe carbonates due to the incorporation of Ca^{2+} ions into siderite structure by replacing Fe^{2+} ions (Figure 4a). Additionally, it is shown that the reflection peaks of Ca-Fe carbonates from Ca-amended sets were broad, indicating that their crystal size is small and perhaps in the nanoscale range. The short XRD scans verified the downward shift of the (104) reflections (Figure 4b). Noticeably, the (104) peak position of the bioreduced product that was obtained from the 20 mM Ca-amended bioreactors was close to that of the ankerite reference (PDF#41-0586) (Figure 4b), suggesting that this Ca-Fe carbonate neoformation had a chemical composition near that of theoretical $CaFe(CO_3)_2$. However, the cation-ordering peaks [e.g., (101) and (015)] were absent in this ankerite-like phase, which suggests that the Ca-Fe arrangement of this mineral was disordered. The ICP-OES data indicated that the carbonates contained 0.03, 10.87, 17.51 and 39.65 mol% $CaCO_3$ from the bioreduction experiments with the starting Ca^{2+} concentrations of 0, 5, 10 and 20 mM, respectively. Because of these chemical similarities, the term “proto-ankerite” is applied herein for

biogenic ankerite-like mineral precipitates obtained from the 20 mM Ca-amended biosystems.

A strong positive correlation was observed between the aforementioned ICP-OES data and the starting Ca^{2+} concentrations (Figure 5a). A similar positive correlation existed for the $CaCO_3$ content in the Ca-Fe carbonates with respect to the *d*-spacing values of (104) reflection (Figure 5b).

3.3.2. Electron microscopic observations

The TEM data revealed that biogenic siderite that formed from the Ca-free systems was 1-2 μm in size and well crystallized in euhedral structure (Figure 6a). Moreover, the corresponding EDS result confirmed the presence of $FeCO_3$ content. In contrast, the obtained Ca-Fe carbonates from the bioreactors with 5 and 10 mM Ca^{2+} possessed coarse structures with a large number of nano-grains (Figure 6b-e). Noticeably, the size of Ca-Fe carbonate that was collected from the 10 mM Ca-amended systems (Figure 6e) was smaller than that from the 5 mM experiments (Figure 6c). High-resolution TEM (HRTEM) image further revealed the dominant $d_{(104)}$ spacing of 0.283 nm for the Ca-Fe carbonate from the 10 mM experiments (Figure 6f), consistent with the XRD data (Figure 5b). The presence of Ca was confirmed by EDS in these Ca-Fe carbonates (Figure 6c and g).

SEM observations of the bioreduced samples from the 20 mM Ca experiments showed the WP3 cells in associated with proto-ankerite particles (Figure 7a). SEM and TEM data collectively revealed that the biogenic proto-ankerite was composed of numerous nano-spheres, with a mean size of 9 nm (Figure 7b-e). As mentioned above,

(101) and (015) are typical cation-ordering reflections for dolomite group minerals. The SAED pattern did not exhibit these superlattice reflections (Figure 7f), which supports the above XRD results. The proto-ankerite phase showed clear lattice fringes, and the width of the fringes was estimated to be 0.286 nm (Figure 7g). This data was in good agreement with the lattice spacing of the (104) plane revealed by XRD measurements (Figure 5b). EDS analyses indicated the signal level of Ca was nearly equal to that of Fe in proto-ankerite phases (Figure 7h). Moreover, a minor amount of Mg was also detected in EDS spectra (Figure 7h). The HRTEM data also revealed that the proto-ankerite contained structural defects. Specifically, the (202) lattice fringes, identified with a *d*-spacing of 0.203 nm, were shown in Figure 8. Based on the inverse fast Fourier transformation (FFT) analysis, a number of stacking faults were revealed within this biogenic mineral precipitate (Figure 8c).

3.4. Transformation of proto-ankerite into ankerite under hydrothermal conditions

After hydrothermal alteration of proto-ankerite in a Mg/Ca saline solution, XRD data showed that the main solid phase was ankerite, along with minor siderite (Figure 9a). In comparison to proto-ankerite, ankerite exhibited significantly sharper XRD peaks and distinctive characteristic reflections of (101), (015) and (021). The ankerite neoformation was blocky and densely packed, and grain size ranged homogeneously between 140 and 170 nm (Figure 9b). As evidenced by EDS, ankerite contained also significant amounts of Mg, Ca and Fe (Figure 9b). ICP-OES measurements can provide more accurate information about the mineral composition. The ICP-OES data indicated

354 that our ankerite sample was composed of 49.8 mol% $CaCO_3$, 27.2 mol% $FeCO_3$, and
355 23 mol% $MgCO_3$. Therefore, its structural formula can be expressed as
356 $CaFe_{0.54}Mg_{0.46}(CO_3)_2$, which is quite close to the ankerite composition
357 [$CaMg_{0.5}Fe_{0.5}(CO_3)_2$] defined by IMA.
358
359 **4. Discussion**
360 **4.1. Effect of Ca^{2+} on microbial reduction of ferrihydrite**
361 Owing to the fact that ferric iron [Fe(III)] is essentially insoluble in neutral pH
362 environments, DIRB face the problem of transferring electrons extracellularly to Fe(III)
363 minerals outside of their cells (Shi et al., 2016). Although DIRB have evolved multiple
364 strategies for utilizing such low solubility electron acceptors, it is a consensus that
365 microbial reduction of Fe(III) minerals is a rate-limiting process, and that the rate of
366 microbial reduction of solid Fe(III) phases can be influenced by a great variety of
367 factors (Roden, 2004; Bonneville et al., 2009). For instance, mineral surface area,
368 particle size and crystallinity have been identified as major mineralogical factors
369 controlling the initial rate of microbial iron reduction (Roden, 2004; Bose et al., 2009;
370 Liu et al., 2012, 2016). In addition to mineralogical factors, several geochemical factors
371 are reported to govern the kinetics of microbial reduction of Fe(III) minerals. For
372 example, quinone-containing compound is known to serve as an electron shuttle to
373 promote microbial iron reduction (Lovley et al., 1996).
374 In the present study, we demonstrated that the presence of Ca^{2+} could accelerate
375 the bioreduction rate with strain WP3 (Figure 2a). Apparently, Ca^{2+} ion lacks the

electron shuttling capability, so there should be some other mechanisms involving the positive effect of Ca^{2+}. It is well documented that in the absence of exogenous electron shuttles, DIRB (e.g., *Shewanella* spp.) primarily employ the mechanism of direct cell-mineral contact to transfer extracellular electrons (Bose et al., 2009). Therefore, the adhesion efficiency of DIRB cells with Fe(III) minerals plays a vital role in bioreduction of Fe(III). Indeed, an experimental study by O'Loughlin et al. (2010) demonstrated that the bioreduction of lepidocrocite was inhibited by phosphate, silicate, and other inorganic oxyanions, due to the competitive adsorption of oxyanions onto lepidocrocite surfaces which can block the access of bacterial cells and reduce bacterial adhesion. Microbial adhesion to mineral surfaces is, at least in part, regulated by electrostatic force (Yee et al., 2000). Normally ferrihydrite is positively charged. However, our Ca-free ferrihydrite suspension had a negative potential (Figure 3), indicating that the ferrihydrite surface developed a net negative charge. This phenomenon might be explained by the coating effect of organic molecules from yeast extract. Due to the existence of high density of ferric hydroxyl functional groups (≡FeOH) on the surface of ferrihydrite, this mineral has a high adsorption capacity for organic molecules (Eusterhues et al., 2011). Noticeably, microbial cell surface is often negatively charged owing to the presence of acidic functional groups such as carboxyl, hydroxyl, and phosphate (Yee et al., 2000). In this regard, a repulsive force existed when WP3 cells interacted with ferrihydrite particles in our systems, which potentially limited the adhesion efficiency and bioreduction rate. When Ca^{2+} ions were introduced into the bioreduction systems, ≡FeOH groups of ferrihydrite could also coordinate

398 with Ca^{2+} ions forming $\equiv[(FeOH)_2Ca]^{2+}$ complexes (Mendez and Hiemstra, 2020). As
399 such, ferrihydrite dispersion tended to become positively charged in the presence of
400 Ca^{2+}, which is validated by its positive zeta potential values (Figure 3). In doing so, an
401 electrostatic attraction between WP3 cells and ferrihydrite particles could occur in the
402 presence of Ca^{2+}, which might account for the enhanced reduction rate in these Ca-
403 amended bio-systems. Although zeta potentials of ferrihydrite suspension gradually
404 increased with increasing Ca concentrations (0-20 mM), almost all of the WP3 cells
405 were already adhered to ferrihydrite in the Ca-amended systems. These adhesion data
406 can interpret the similar bioreduction rates observed in Ca-amended systems (Figure
407 2a).

408 The final extents of Fe(III) reduction for the bioreactors were in the range of 76.4-
409 83.5%. These data demonstrated that the bioreduction of ferrihydrite by strain WP3 was
410 an incomplete process. Owing to excessive lactate used in our experiments, this
411 incomplete bioreduction was not the result of insufficient electron donation. In fact,
412 similar results have been observed for other DIRB such as *S. putrefaciens* CN32
413 (Fredrickson et al., 1998) and *S. oneidensis* MR-1 (Amstaetter et al., 2012). According
414 to previous experimental studies, the incomplete bioreduction of Fe(III)-containing
415 minerals is mainly ascribed to the blocking effect of produced Fe(II) (Roden and Urrutia,
416 1999; Urrutia et al., 1999). During bioreduction, a considerable amount of Fe(II) ions
417 can be released into aqueous solutions (Figure 2b). These produced Fe(II) ions are
418 preferentially adsorbed onto Fe(III)-containing minerals and cell surfaces, leading to
419 the blockage of active surface sites (Roden and Urrutia, 1999). In addition, mineral

aggregation has also been thought to inhibit the long-term bioreduction (Urrutia et al., 1999). As evidenced by our microscopic data, the neoformed Ca-Fe carbonates were shown to be in aggregate form (Figures 6 and 7). Noticeably, WP3 cells were embedded in the neoformed aggregates (Figure 7a). It is reasonable to speculate that the Ca-Fe carbonate neoformations might physically block the microbial extracellular electron transfer.

4.2. Formation mechanism of Ca-Fe carbonate mediated by *S. piezotolerans* WP3

It has been well documented that microbial reduction of Fe(III) oxides can result in formation of secondary Fe(II)-bearing minerals, such as siderite, vivianite, magnetite, green rust, and chukanovite (Fredrickson et al., 1998; Ona-Nguema et al., 2002; O'Loughlin et al., 2010; Wu et al., 2011). The rate of Fe(II) production and aqueous chemical composition are two crucial parameters in regulating the crystallization of specific Fe(II) phases (Fredrickson et al., 1998; O'Loughlin et al., 2010). Specifically for siderite, it is a common mineral product observed in the bioreduction systems with a high production rate of Fe(II) and high alkalinity (Fredrickson et al., 1998). In the present study, the medium used for bioreduction experiments contained high amounts of dissolved inorganic carbon (DIC; 30 mM HCO_3^-). Microbial mineralization of organic sources of carbon (e.g., lactate used herein) can also enhance the concentration of DIC. Furthermore, as evidenced by ammonium production (Figure 1), strain WP3 had the ability to ammonify the nitrogen sources in yeast extract. Specifically, only a slight rise in pH was observed for the abiotic reactors (Figure 1a), which might be caused by the protonation of hydroxyl and(or) carboxyl sites within yeast extract.

442 However, sharper increases in pH as well as alkalinity occurred in the bioreactors
443 (Figure 1a). These significant changes observed in the bioreduction systems might be
444 attributed to microbial ammonification (yeast extract → NH_3+H_2O → NH_4^+ + OH^-).
445 Taken together, the concentration of CO_3^{2-} could be significantly elevated due to DIC
446 partitioning under an alkaline environment, thus providing oversaturated conditions for
447 siderite when Fe^{2+} ions were present in aqueous solutions (Figure 2). Aforementioned
448 results can explain the occurrence of siderite in our Ca-free systems.

449 When Ca^{2+} ions were introduced in our bioreduction systems, Ca-Fe carbonate
450 neoformations occurred and their $CaCO_3$ content was highly dependent on the starting
451 concentration of Ca^{2+} in solutions. Given the fact that the charge density and ionic
452 radius of Ca^{2+} are similar to those of Fe^{2+}, the Fe^{2+} sites in the lattice of siderite can be
453 theoretically substituted by Ca^{2+} ions (Romanek et al., 2009). Indeed, cation-disordered
454 phases in the $(Ca,Fe)CO_3$ have been successfully synthesized at low temperatures.. For
455 instance, Romanek et al. (2009) reported that the Ca-Fe carbonates that were
456 inorganically synthesized at 25 °C had the $CaCO_3$ content less than 17 mol% (Romanek
457 et al., 2009). Our present study showed that strain WP3 was capable of facilitating the
458 loading of Ca^{2+} during Ca-Fe carbonate growth at 20 °C. The $CaCO_3$ content of our Ca-
459 Fe carbonates was estimated up to 39.65 mol%. This value is much higher than that of
460 low-temperature inorganic counterparts mentioned above. Such apparent discrepancy
461 might be attributed to the high aqueous Ca/Fe ratio observed in our bioreduction
462 systems. Specifically, the Ca/Fe molar ratio of experimental solutions using by
463 Romanek et al. (2009) was within the range of 0.03-1.05. Although the concentrations

of aqueous Fe(II) in all bioreactors increased as a consequence of microbial reduction of ferrihydrite (Figure 2b), the average Ca/Fe molar ratio was still as high as 8.36, 14.09 and 28.65 for the bioreactors with 5, 10 and 20 mM Ca^{2+}, respectively. Apparently, a solution with high Ca/Fe ratios can provide sufficient Ca^{2+} for the growth of Ca-Fe carbonates.

It is relevant to note that both Ca^{2+} and Fe^{2+} are typically hydrated in solutions (Lippmann, 1973). As such, there exists an energy barrier against the hydration shell of these cations, blocking the approach of CO_3^{2-} ions to either Ca^{2+} or Fe^{2+} ions. This hydration effect can be diminished at high temperature when the thermal energy exceeds the energy barrier variations, whereas it persists at ambient temperature (Romanek et al., 2009).The occurrence of low-temperature biogenic Ca-Fe carbonates showed that strain WP3 had a positive effect on dehydration of Ca^{2+} and Fe^{2+}. Actually, the catalytic role of microorganisms in dehydration of metal ions has been long recognized and interpreted as suggesting that the negatively-charged groups (especially carboxyl) on microbial cells break down the hydration shell of metal ions via electrostatic forces (de Vasquez et al., 2021). In general, carboxyl and other acidic groups preferentially interact with metal ions to form cation-organic complexes, accompanied by the partial removal of the outer shell water around the metal cations (Qiu et al., 2017; Huang et al., 2019). According to the study reported by Huang et al. (2019), strain WP3 has a high density of cell surface-bound carboxyl groups (0.057 $Å^{-2}$), which is significantly higher than non-marine DIRB (0.03 $Å^{-2}$) (Kenward et al.,

2013). Therefore, it is reasonable to speculate that WP3 cells can lower the energy barrier to the incorporation of Ca^{2+} and Fe^{2+} into growing Ca-Fe carbonates.

Besides Ca ions, our bioreduction medium also contained considerable amounts of Mg^{2+}. However, as evidenced by the new EDS data, only trace amounts of Mg were detected in the Ca-Fe carbonates (Figure 7h), which is consistent with a previous study that showed the formation of a $(Ca,Fe)CO_3$ phase rather than $(Ca,Mg,Fe)CO_3$ in bioreduced systems with ferric hydroxide, a non-marine DIRB (*S. oneidensis* MR-1), as well as Ca^{2+} and Mg^{2+} ions (Zeng and Tice, 2014). Thus, these results demonstrate that Ca^{2+} is more effective than Mg^{2+} in competing for the substitution of Fe. Such phenomenon is likely accounted for by the difference in dehydration enthalpy of Ca^{2+} vs. Mg^{2+}. Numerous computational studies have demonstrated that Mg^{2+} has the higher dehydration enthalpy than Ca^{2+} (351.8 kcal/mole vs. 264.3 kcal/mole) (Jiao et al., 2006), owing to longer lifetime of water molecules around Mg^{2+} and higher surface charge density of this cation (Jiao et al., 2006; Romanek et al., 2009). As a result, more energy is required for the dissociation of Mg-H_2O complexes compared to Ca-H_2O complexes, and thus Mg incorporation in the Ca-Fe carbonate structure is quite limited at low temperature.

4.3. Proto-ankerite and its transformation

The Ca-Fe carbonate produced from the 20 mM Ca-amended bioreactors had an average $CaCO_3$ content of 39.65 mol%, that is, with a chemical formula of $Ca_{0.8}Fe_{1.2}(CO_3)_2$. This chemical composition is close to that of "theoretical" ankerite [$CaFe(CO_3)_2$]. However, as mentioned earlier, our ankerite-like neoformation lacked

507 Ca-Fe ordering as evidenced by XRD and SAED data. Not limited to aforementioned
508 ankerite-like phase, the synthesis of other disordered double carbonates has also been
509 achieved under ambient conditions due to the presence of microbial activity. Disordered
510 dolomite is a good example with new recent advances. A growing number of studies
511 reveal that various types of microbes can facilitate the precipitation of Ca-Mg
512 carbonates at Earth surface temperatures (e.g., Vasconcelos et al., 1995; Sánchez-
513 Román et al., 2008; Bontognali et al., 2012; Qiu et al., 2017; Huang et al., 2019; Liu et
514 al., 2019, 2020; Zhang et al., 2021; Han et al., 2022). The Mg level of these microbially-
515 induced Ca-Mg carbonates is generally above 10 mol% and reaches up to 48 mol%.
516 According to the definition of Graf and Goldsmith (1956), the Ca-Mg carbonate having
517 near-dolomite stoichiometry (≥36 mol% $MgCO_3$) but disordered Ca-Mg arrangement
518 should be termed "proto-dolomite". A number of laboratory experiments have
519 demonstrated that proto-dolomite can convert into dolomite during burial diagenesis
520 (Malone et al., 1996; Rodriguez-Blanco et al., 2015; Kaczmarek and Thornton, 2017;
521 Zheng et al., 2021). Motivated by these studies, herein we introduce the term "proto-
522 ankerite" to describe Ca-Fe carbonate which is of approximately ankeritic composition
523 but lacks Ca-Fe order.

524 It is a general consensus that nanominerals are highly reactive due to their high
525 surface-to-volume ratio (Hochella Jr. et al., 2008). Our proto-ankerites were in the range
526 of a few nanometers (Figure 7). It has been also reported that some microbially-
527 mediated minerals (e.g., ZnS) have much more defective crystalline structures
528 compared to their abiotic counterparts (e.g., Xu et al., 2016). In the new experiments,

TEM data revealed that planar defects were also present in low-temperature proto-ankerite (Figure 8). These nano-scale and defect-rich properties should allow microbially-induced ankerite to be unstable in open diagenetic environments where intense alterations triggered by external fluid take place. Indeed, our hydrothermal experiments showed that the proto-ankerite was converted into ankerite at 100 °C in a Mg/Ca-containing saline solution, demonstrating that microbially-mediated proto-ankerite can serve as a precursor for sedimentary ankerite. Unlike Mg-poor nature of proto-ankerite, the newly-formed ankerite had equal amounts of Mg and Fe (Figure 9b). These results suggested that high temperatures can lower the activation barrier for Mg^{2+} dehydration and that Mg incorporation in ankerite is achieved by the substitution of Mg for Fe. Indeed, siderite was found to accompany the hydrothermal transformation of proto-ankerite to ankerite (Figure 9a), which can serve as indirect evidence for the release of Fe^{2+} from proto-ankerite due to Mg substitution.

Many ankerite cements are commonly found in shallow marine sandstone reservoirs (e.g., Kantorowicz, 1985; Hendry et al., 2000), and most were thought to be early diagenetic and authigenic in origin (Kantorowicz, 1985). It is noted that those ankerite cements had negative $\delta^{13}C$ values. For instance, ankerite cements from the Wilcox Group in southwest Texas had $\delta^{13}C$ values from -5.2 to -9.0‰ PDB (Kantorowicz, 1985). These $\delta^{13}C$ signatures may be related to the microbial oxidation of organic substrates. Moreover, siderite was frequently observed to co-exist with ankerite in aforementioned settings. On the basis of our cultivation and precipitation experiments, as well as published field studies, we propose that microbial iron reduction

551 can contribute to the genesis of sedimentary ankerite (Figure 10). Similar to the
552 recognized mediation of microorganisms in the precipitation of dolomite,
553 microorganisms facilitate the formation of ankerite by providing a metastable, low-
554 temperature carbonate precursor, which can be converted into ordered counterpart upon
555 diagenesis and hydrothermal alteration.
556
557 **5. Conclusions**
558 Through laboratory experiments we demonstrated the formation of Ca-Fe
559 carbonates from bioreduction of ferrihydrite by *S. piezotolerans* WP3 in a bicarbonate-
560 buffered, Ca^{2+}-amended medium. The content of $CaCO_3$ in the neoformed Ca-Fe
561 carbonates was positively correlated with the initial concentration of Ca^{2+} within the
562 medium. Microbially-induced proto-ankerite having 39.65 mol% $CaCO_3$ was observed
563 when the concentration of Ca^{2+} was up to 20 mM. Our proto-ankerite was nanoscopic
564 in size, spherical in shape, cation-disordered, and with a defective crystalline structure.
565 The hydrothermal experiments provided evidence that ordered ankerite can be
566 produced through the recrystallization of biogenic proto-ankerite at 100 °C. The
567 conversion of proto-ankerite to ankerite was triggered by the substitution of Mg^{2+} for
568 Fe^{2+} in the lattice structure, leading to solubilization of excess Fe and concomitant
569 siderite precipitation.
570
571 **Acknowledgments**

This research was jointly supported by the National Natural Science Foundation of China (Nos. 42272046, 42293292 and 42072336), National Key R&D Program of China (2022YFF0800304), and the 111 Project (No. BP0820004). The authors are grateful to the handling editor and two anonymous reviewers whose comments improved the quality of this manuscript.

References

Amstaetter K, Borch T, Kappler A. 2012. Influence of humic acid imposed changes of ferrihydrite aggregation on microbial Fe(III) reduction. Geochim Cosmochim Acta, 85: 326-341

Bonneville S, Behrends T, van Cappellen P. 2009. Solubility and dissimilatory reduction kinetics of iron(III) oxyhydroxides: A linear free energy relationship. Geochim Cosmochim Acta, 73: 5273-5282

Bontognali T R R, Vasconcelos C, Warthmann R J, Lundberg R, McKenzie J A. 2012. Dolomite-mediating bacterium isolated from the sabkha of Abu Dhabi (UAE). Terra Nova 24: 248-254

Bose S, Hochella Jr M F, Gorby Y A, Kennedy D W, McCready D E, Madden A S, Lower B H. 2009. Bioreduction of hematite nanoparticles by the dissimilatory iron reducing bacterium *Shewanella oneidensis* MR-1. Geochim Cosmochim Acta 73: 962-976

Chang B, Li C, Liu D, Foster I, Tripati A, Lloyd M K, Maradiaga I, Luo G, An Z, She Z, Xie S, Tong J, Huang J, Algeo T J, Lyons T W, Immenhauser A. 2020. Massive

formation of early diagenetic dolomite in the Ediacaran ocean: Constraints on the "dolomite problem". Proc Natl Acad Sci U S A 117: 14005-14014

Eusterhues K, Rennert T, Knicker H, Kögel-Knabner I, Totsche K U, Schwertmann U. 2011. Fractionation of organic matter due to reaction with ferrihydrite: Coprecipitation versus adsorption. Environ. Sci. Technol. 45: 527-533

Fredrickson J K, Zachara J M, Kennedy D W, Dong H, Onstott T C, Hinman N W, Li S. 1998. Biogenic iron mineralization accompanying the dissimilatory reduction of hydrous ferric oxide by a groundwater bacterium. Geochim Cosmochim Acta 62: 3239-3257

Graf D L, Goldsmith J R. 1956. Some hydrothermal syntheses of dolomite and protodolomite. J Geol 64: 173-186

Gregg J M, Bish D L, Kaczmarek S E, Machel H G. 2015. Mineralogy, nucleation and growth of dolomite in the laboratory and sedimentary environment: a review. Sedimentology 62: 1749-1769

Guo C, Chen D, Dong S, Qian Y, Liu C. 2017. Early dolomitisation of the Lower-Middle Ordovician cyclic carbonates in northern Tarim Basin, NW China. Sci China Earth Sci 60: 1283-1298

Han Z, Qi P, Zhao Y, Guo N, Yan H, Tucjer M E, Li D, Wang J, Zhao H. 2022. High Mg/Ca molar ratios promote protodolomite precipitation induced by the extreme halophilic bacterium Vibrio harveyi QPL2. Front Microbiol 13: 821968

Hendry J P, Wilkinson M, Fallick A E, Haszeldine R S. 2000. Ankerite cementation in deeply buried Jurassic sandstone reservoirs of the central North Sea. J Sediment

Res 70: 227-239

Higgins J A, Blattler C L, Lundstrom E A, Santiago-Ramos D P, Akhtar A A, Ahm A C, Bialik O, Holmden C, Bradbury H, Murray S T, Swart P K. 2018. Mineralogy, early marine diagenesis, and the chemistry of shallow-water carbonate sediments. Geochim Cosmochim Acta 220: 512-534

Hochella Jr M F, Lower S K, Maurice P A, Pen R L, Sahai N, Sparks D L, Twining B S. 2008. Nanominerals, mineral nanoparticles, and Earth systems. Science 319: 1631-1635

Huan Y, Yao Q, Li H, Wang F, Zhou G, Fu S. 2019. Aerobically incubated bacterial biomass-promoted formation of disordered dolomite and implication for dolomite formation. Chem Geol 523: 19-30

Jiao D, King C, Grossfield A, Darden T A, Ren P. 2006. Simulation of Ca^{2+} and Mg^{2+} solvation using polarizable atomic multipole potential. J Phys Chem B 110: 18553-18559

Kaczmarek S E, Thornton B P. 2017. The effect of temperature on stoichiomety, cation ordering, and reaction rate in high-temperature dolomitization experiments. Chem Geol 468: 32-41

Kantorowicz J D. 1985. The origin of authigenic ankerite from the Ninian Field, UK North Sea. Nature 315: 214-216

Kenward P A, Fowle D A, Goldstein R H, Ueshima M, González L A, Roberts J A. 2013. Ordered low-temperature dolomite mediated by carboxyl-group density of microbial cell walls. AAPG Bull 97: 2113-2125

638 Kukkadapu R K, Zachara J M, Fredrickson J K, Kennedy D W. 2004. Biotransformation
639 of two-line silica-ferrihydrite by a dissimilatory Fe(III)-reducing bacterium:
640 formation of carbonate green rust in the presence of phosphate. Geochim
641 Cosmochim Acta 68: 2799-2814
642 Li M, Wignall P B, Dai X, Hu M, Song H. 2021. Phanerozoic variation in dolomite
643 abudance linked to oceanic anoxia. Geology 49: 698-702
644 Lippmann F. 1973. Crystal chemistry of sedimentary carbonate minerals, Sedimentary
645 Carbonate Minerals. Springer pp. 5-96
646 Liu C, Li W. 2020. Transformation of amorphous precursor to crystalline carbonate:
647 Insights from Mg isotopes in the dolomite-analogue mineral norsethite
648 [$BaMg(CO_3)_2$]. Geochim Cosmochim Acta 272: 1-20
649 Liu D, Dong H, Bishop M E, Zhang J, Wang H, Xie S, Wang S, Huang L, Eberl D D.
650 2012. Microbial reduction of structural iron in illite-smectite minerals by a sulfate-
651 reducing bacterium. Geobiology 10: 150-162
652 Liu D, Yu N, Papineau D, Fan Q, Wang H, Qiu X, She Z, Luo G. 2019. The catalytic
653 role of planktonic aerobic heterotrophic bacteria in protodolomite formation:
654 Results from Lake Jibuhulangtu Nuur, Inner Mogolia, China. Geochim Cosmochim
655 Acta 263: 31-49
656 Liu D, Fan Q, Papineau D, Yu N, Chu Y, Wang H, Qiu X, Wang X. 2020. Precipitation
657 of protodolomite facilitated by sulfate-reducing bacteria: The role of capsule
658 extracellular polymeric substances. Chem Geol 533: 119415
659 Liu Y, Chen C, He D, Chen W. 2019. Deep carbon cycle in subduction zones. Sci China

660 Earth Sci 62: 1764-1782
661 Lovley D R, Coates J D, Blunt-Harris E L, Phillips E J P, Woodward J C. 1996. Humic
662 substances as electron acceptors for microbial respiration. Nature 382: 445-447
663 Malone M J, Baker P A, Burns S J. 1996. Recrystallization of dolomite: An
664 experimental study from 50-200°C. Geochim Cosmochim Acta 60: 2189-2207
665 Marin F, Smith M, Isa Y, Muyzer G, Wstbroek P. 1996. Skeletal matrices, muci, and the
666 origin of invertebrate calcification. Proc Natl Acad Sci U S A 93: 1554-1559
667 Mendez J C, Hiemstra T. 2020. Ternary complex formation of phosphate with Ca and
668 Mg ions binding to ferrihydrite. ACS Earth Space Chem. 4: 545-557
669 McLeod S. 1992. Micro-distillation unit for use in continuous flow analyzers. Its
670 construction and use in determination of ammonia and nitrate in soils. Anal Chim
671 266: 107-112
672 O'Loughlin E J, Gorski C, Scherer M M, Boyanov MI, Kemner K M. 2010. Effects of
673 oxyanions, natural organic matter, and bacterial cell numbers on the bioreduction
674 of lepidocrocite (γ-FeOOH) and the formation of secondary mineralization products.
675 Environ Sci Technol 44: 4570-4576
676 Ona-Nguema G, Abdelmoula M, Jorand F, Benali O, Block J, Cénin J R. 2002. Iron (II,
677 III) hydroxycarbonate green rust formation and stabilization from lepidocrocite
678 bioreduction. Environ Sci Technol: 36, 16-20
679 Perri E, Tucker M. 2007. Bacterial fossils and microbial dolomite in Triassic
680 stromatolites. Geology 35: 207-210
681 Petrash D A, Bialik O M, Bontognali T R R, Vasconcelos C, Roberts J A, McKenzie J

682 A, Konhauser K O. 2017. Microbially catalyzed dolomite formation: From near-
683 surface to burial. Earth-Sci Rev 171: 558-582
684 Pimentel C, Pina C M. 2016. Reaction pathways towards the formation of dolomite-
685 analogues at ambient conditions. Geochim Cosmochim Acta 178: 259-267
686 Qiu X, Wang H, Yao Y, Duan Y. 2017. High salinity facilitates dolomite precipitation
687 mediated by *Haloferax volcanii* DS52. Earth Planet Sci Lett 472: 197-205
688 Roden E E, Urrutia M M. 1999. Ferrous iron removal promotes microbial reduction of
689 crystalline iron(III) oxides. Environ Sci Technol 33 1847-1853
690 Roden E E, Leonardo M R, Ferris F G. 2002. Immobilization of strontium during iron
691 biomineralization coupled to dissimilatory hydrous ferric oxide reduction. Geochim
692 Cosmochim Acta 66: 2823-2839
693 Roden E E. 2004. Analysis of long-term bacterial vs. chemical Fe(III) oxide reduction
694 kinetics. Geochim Cosmochim Acta 68: 3205-3216
695 Rodriguez-Blanco J D, Shaw S, Benning L G. 2015. A route for the direct crystallization
696 of dolomite. Am Mineral 100: 1172-1181
697 Romanek C S, Jiménez-López C, Navarro A R, Sánchez-Román M, Sahai N, Coleman,
698 M. 2009. Inorganic synthesis of Fe-Ca-Mg carbonates at low temperature. Geochim
699 Cosmochim Acta 73: 5361-5376
700 Sánchez-Román M, Vasconcelos C, Schmid T, Dittrich M, McKenzie J A, Zenobi R,
701 Rivadeneyra M A. 2008. Aerobic microbial dolomite at the nanometer scale:
702 Implications for the geologic record. Geology 36: 879-882
703 Sarazin G, Michard G, Prevot F. 1999. A rapid and accurate spectroscopic method for

alkalinity measurements in sea water samples. Water Res 33: 290-294

Schwertmann U, Cornell R M. 1991. Iron Oxides in the Laboratory: Preparation and Characterization. VCH Publishers, Inc, New York.

Shi L, Dong H, Reguera G, Beyenal H, Lu A, Liu J, Yu H, Fredrickson J K. 2016. Extracellular electron transfer mechanisms between microorganisms and minerals. Nat Rev Microbiol 14: 651-662

Schrag D P, Higgins J A, Macdonald F A, Johnston D T. 2013. Authigenic carbonate and the histroy of the global carbon cycle. Science 339: 540-543

Stookey L L. 1970. Ferrozine-A new spectrophotometric reagent for iron. Anal Chem 42: 779-781

Urrutia M M, Roden E E, Zachara J M. 1999. Influence of aqueous and solid-phase Fe(II) complexants on microbial reduction of crystalline iron(III) oxides. Environ Sci Technol 33: 4022-4028

Vasconcelos C, McKenzie J A, Bernasconi S, Grujic D, Tiens A J. 1995. Microbial mediation as a possible mechanism for natural dolomite formation at low temperatures. Nature 377: 220-222

Wang F, Wang J, Jian H, Zhang B, Li S, Wang F, Zeng X, Gao L, Bartlett D H, Yu J, Hu S, Xiao X. 2008. Environmental adaptation: genomic analysis of the piezotolerant and psychrotolerant deep-sea iron-reduing bacterium *Shewanella piezotolerans* WP3. Plos One 3: 1-12

Wen Y, Sánchez-Román M, Li Y, Wang C, Han Z, Zhang L, Gao Y. 2020. Nucleation and stabilization of Eocene dolomite in evaporative lacustrine deposits from central

726 Tibetan plateau. Sedimentology 67: 3333-3354
727 Wu W, Li B, Hu J, Li J, Wang F, Pan Y. 2011. Iron reduction and magnetite
728 biomineralization mediated by a deep-sea iron-reducing bacterium *Shewanella*
729 *piezotolerans* WP3. J Geophys Res 116: G04034
730 Xie S, Liu D, Qiu X, Huang X, Algeo T J. 2016. Microbial roles equivalent to geological
731 agents of high temperature and pressure in deep Earth. Sci China Earth Sci 59:
732 2098-2104
733 Xu J, Murayama M, Roco C M, Veeramani H, Michel F M, Rimstidt J D, Winkler C,
734 Hochella Jr, M F. 2016. Highly-defective nanocrystals of ZnS formed via
735 dissimilatory bacterial sulfate reduction: A comparative study with their abiogenic
736 analogues. Geochim Cosmochim Acta: 180, 1-14
737 Xu F, You X, Li Q, Liu Y. 2019. Can primary ferroan dolomite and ankerite be
738 precipitated? Its implications for formation of submarine methane-derived
739 authigenic carbonate (MDAC) chimney. Minerals 9: 413
740 Yee N, Fein J B, Daughney C J. 2000. Experimental study of the pH, ionic strength,
741 and reversibility behavior of bacteria-mineral adsorption. Geochim Cosmochim
742 Acta 64: 609-617
743 You X, Sun S, Zhu J. 2014. Significance of fossilized microbes from the Cambrian
744 stromatolites in the Tarim Basin, Northwest China. Sci China Earth Sci 57: 2901-
745 2913
746 Zeng Z, Tice M M. 2014. Promotion and nucleation of carbonate precipitation during
747 microbial iron reduction. Geobiology 12: 362-371

748 Zhang F, Xu H, Konishi H, Shelobolina E S, Roden E. 2012. Polysaccharide-catalyzed
749 nucleation and growth of disordered dolomite: A potential precursor of sedimentary
750 dolomite. Am Mineral 97: 556-567
751 Zhang F, Xu H, Shelobolina E S, Konishi H, Roden E E. 2021. Precipitation of low-
752 temperature disordered dolomite induced by extracellular polymeric substances of
753 methanogenic archaea *Methanosarcina barkeri*: Implications for sedimentary
754 dolomite formation. Am Mineral 106: 69-81
755 Zhao W, Walker S L, Huang Q, Cai P. 2014. Adhesion of bacterial pathogens to soil
756 colloidal particles: Influences of cell type, natural organic matter, and solution
757 chemistry. Water Res 53: 35-46
758 Zheng W, Liu D, Yang S, Fan Q, Papineau D, Wang H, Qiu X, Chang B, She Z. 2021.
759 Transformation of protodolomite to dolomite proceeds under dry-heating
760 conditions. Earth Planet Sci Lett 576: 117249

761 **Figure caption:**

762 **Figure 1.** Time course analysis of solution during microbial reduction of ferrihydrite:
763 (a) solution pH; (b) cell number (CFU); (c) NH_4^+; and (d) solution alkalinity. All results
764 were from duplicate cultures.

765

766 **Figure 2.** Time course change of concentration of total Fe(II) (a), aqueous Fe(II) (b),
767 aqueous Mg (c) and aqueous Ca (d) during microbial iron reduction.

768

769 **Figure 3.** Zeta potential of ferrihydrite suspension in the presence of Ca^{2+} at different
770 pHs. The plot shows systematically higher Zeta potentials for higher Ca^{2+}
771 concentrations.

772

773 **Figure 4.** (a) Comparison XRD patterns between secondary mineral products after 50
774 days of bioreduction and homogeneous in-house standards of iron-bearing minerals
775 (ankerite and siderite); (b) Comparison of diagnostic XRD peaks in 2θ range of 30.5-
776 32.5° for the (104) plane. Note the broadening of peaks as well as their shift towards
777 lower angles and smaller separation for experiments with higher Ca^{2+} concentrations.

778

779 **Figure 5.** (a) Linear relationship between initial Ca^{2+} in medium and $CaCO_3$ content of
780 Ca-Fe carbonate neoformations; (b) Relationship between $CaCO_3$ content of Ca-Fe
781 carbonates and their $d_{(104)}$ values.

782

Figure 6. TEM images of secondary mineral products after bioreduction (day 50): (a) prismatic habit siderite produced in the Ca-free bioreactors. The insert EDS data shows the chemical composition of biogenic siderite, with contaminant Cu peaks from the TEM grid; (b) Anhedral Ca-Fe carbonates from the 5 mM Ca-amended bioreactors; (c) An enlarged view of the square of B showing the nano-sized aggregates and their chemical composition; (d-g) The morphology, predominant lattice fringes, and chemical composition of Ca-Fe carbonates produced in the biosystems with 10 mM Ca^{2+}.

Figure 7. SEM (a-b) and TEM (c-g) images of proto-ankerite nanoparticle collected by the end of experiments (50 days) from the bioreactors with 20 mM Ca^{2+}.

Figure 8. (a) HRTEM image showing the lattice fringes of microbially-induced proto-ankerite obtained after the bioreduction systems for 50 days; (b) The lattice spacing distribution of the selected area in the panel A; (c) The inverse FFT of the square area in the panel A showing the stacking faults.

Figure 9. (a) XRD results showing the differences between pristine and hydrothermal-treated proto-ankerite, where the peaks in the pristine proto-ankerite are significantly broader than in the hydrothermal experiment; (b) SEM image and EDS data of ordered ankerite from a two-month hydrothermal experiments.

805 **Figure 10.** Proposed model illustrating the role of iron-reducing microbes on the
806 formation of ankerite.

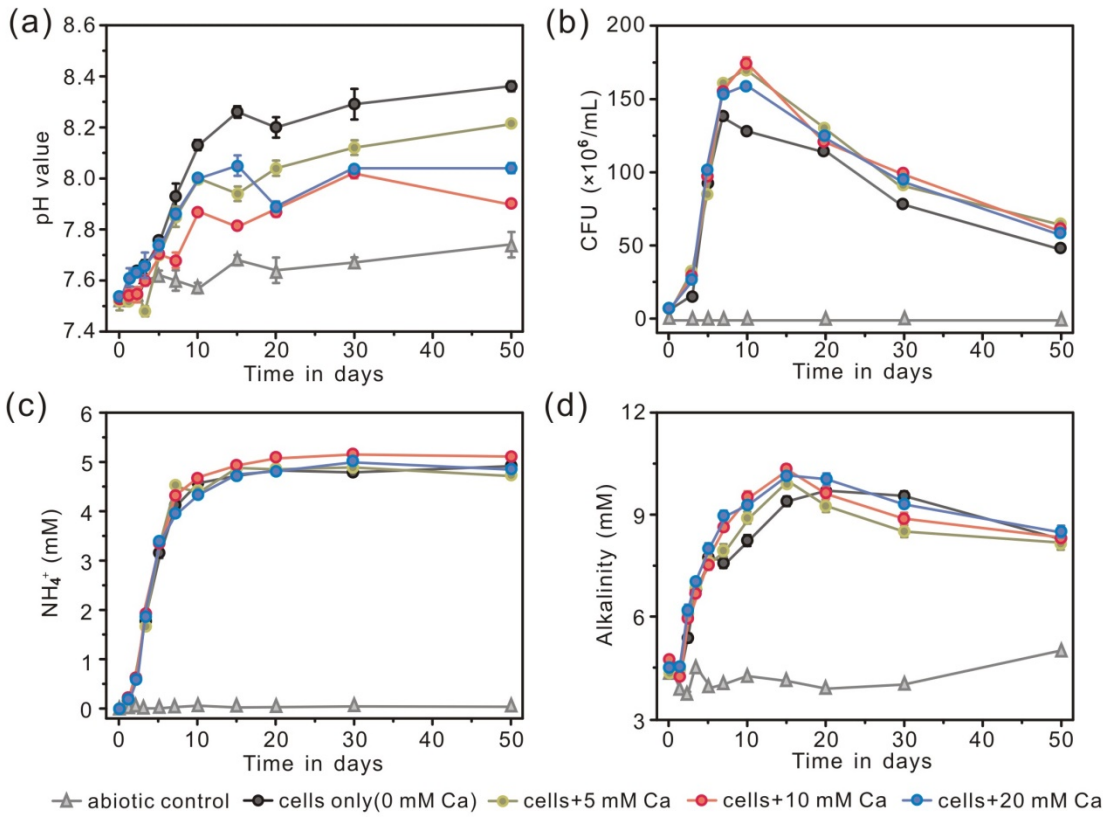
(a)
pH value
Time in days
(b)
CFU (×10⁶/mL)
Time in days
(c)
NH₄⁺ (mM)
Time in days
(d)
Alkalinity (mM)
Time in days
abiotic control
cells only(0 mM Ca)
cells+5 mM Ca
cells+10 mM Ca
cells+20 mM Ca

Figure 1

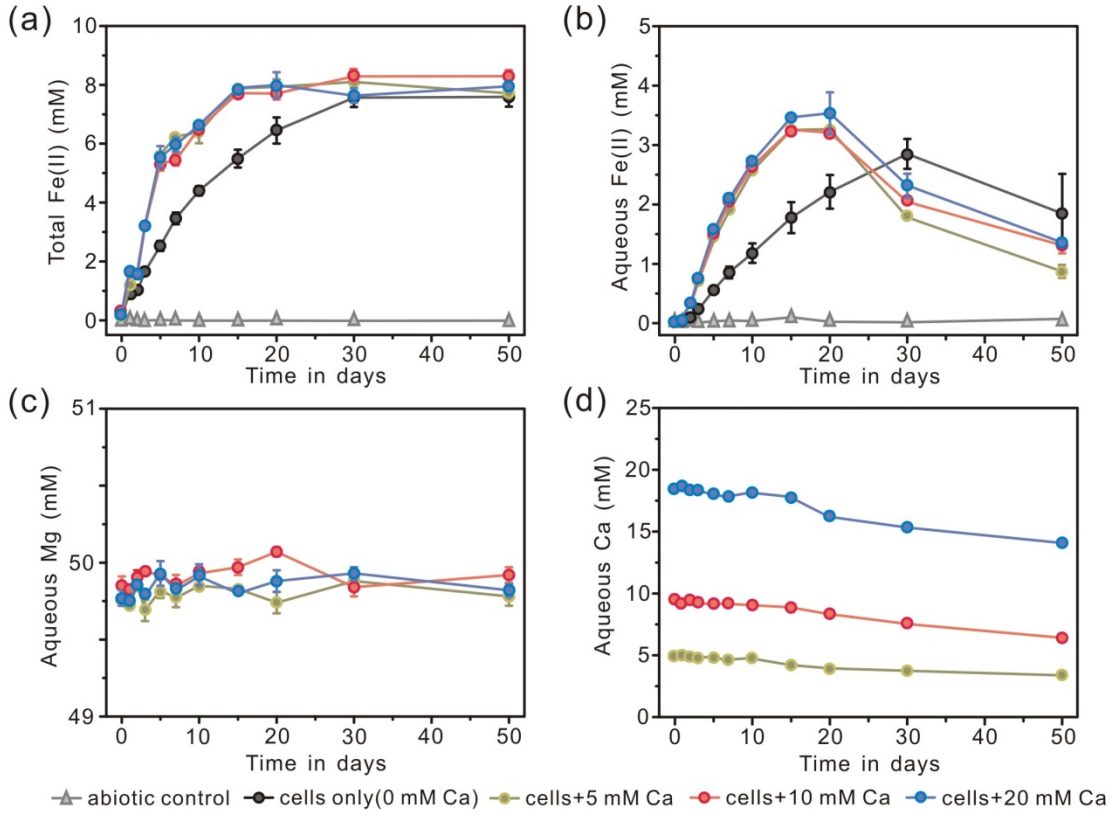
(a)
Total Fe(II) (mM)
Time in days
(b)
Aqueous Fe(II) (mM)
Time in days
(c)
Aqueous Mg (mM)
Time in days
(d)
Aqueous Ca (mM)
Time in days
abiotic control
cells only(0 mM Ca)
cells+5 mM Ca
cells+10 mM Ca
cells+20 mM Ca

Figure 2

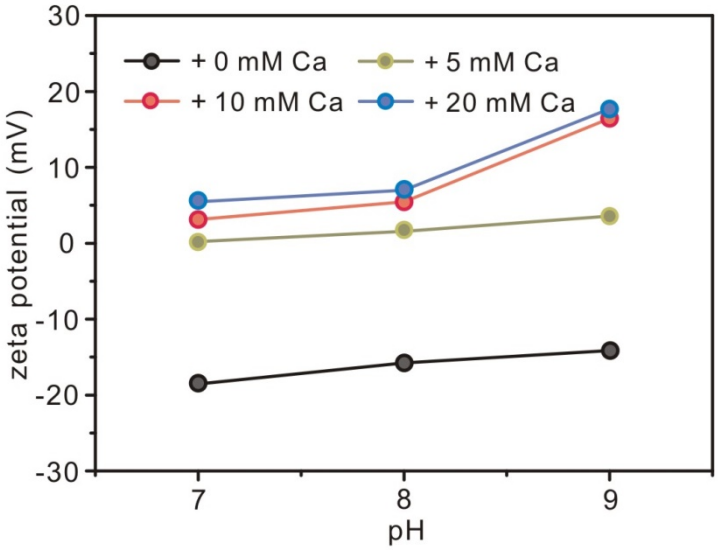
30
20
10
0
-10
-20
-30
zeta potential (mV)
+ 0 mM Ca
+ 5 mM Ca
+ 10 mM Ca
+ 20 mM Ca
7
8
9
pH

Figure 3

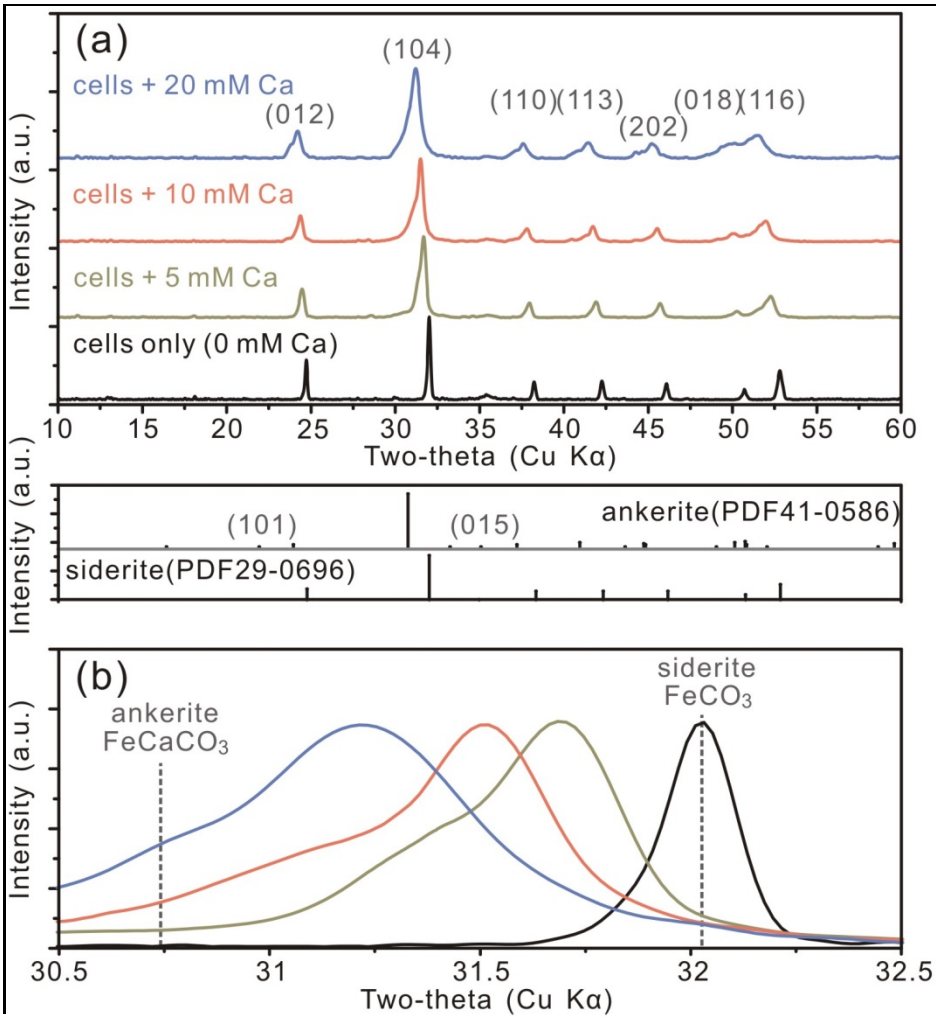
(a)
cells + 20 mM Ca
cells + 10 mM Ca
cells + 5 mM Ca
cells only (0 mM Ca)
(012)
(104)
(110)
(113)
(202)
(018)
(116)
Intensity (a.u.)
10 15 20 25 30 35 40 45 50 55 60
Two-theta (Cu Kα)
(101)
(015)
ankerite(PDF41-0586)
siderite(PDF29-0696)
Intensity (a.u.)
(b)
ankerite
FeCaCO3
siderite
FeCO3
Intensity (a.u.)
30.5 31 31.5 32 32.5
Two-theta (Cu Kα)

Figure 4

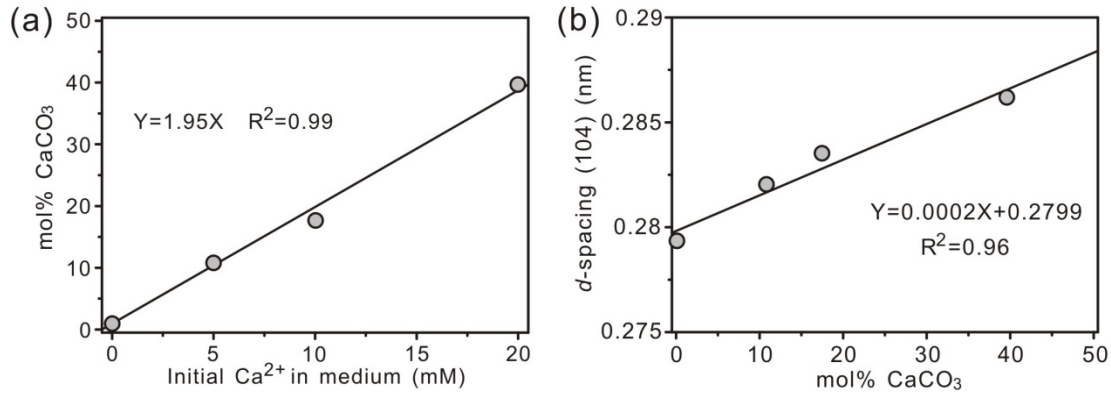
(a)
mol% CaCO3
Y=1.95X R2=0.99
Initial Ca2+ in medium (mM)
(b)
d-spacing (104) (nm)
Y=0.0002X+0.2799
R2=0.96
mol% CaCO3

Figure 5

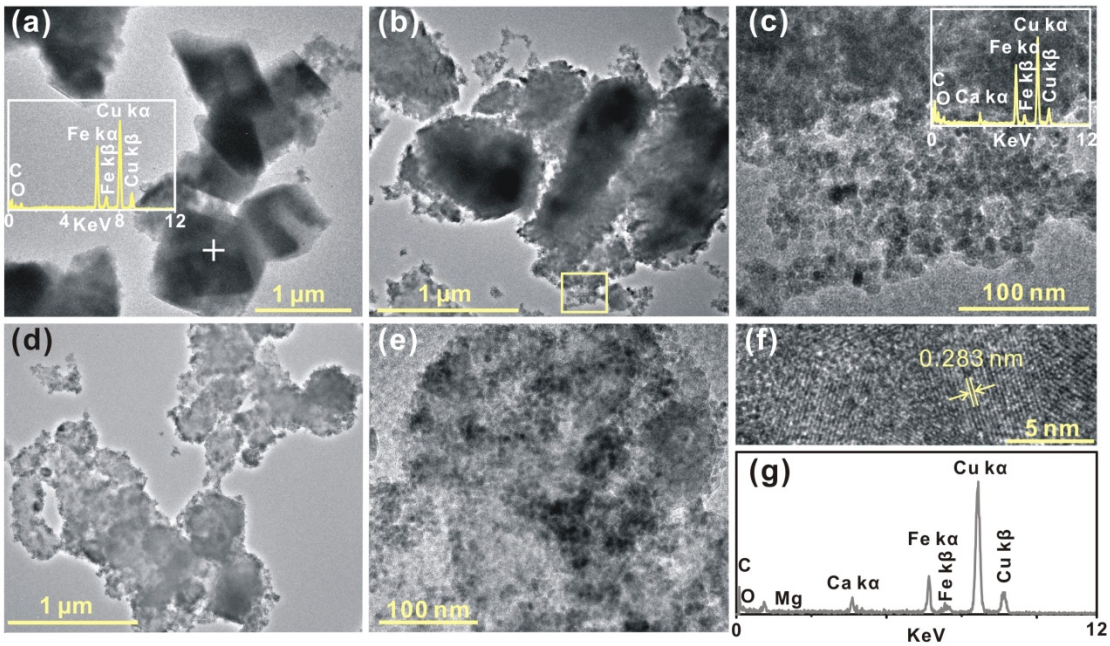
(a)
Cu kα
Fe kα
Fe kβ
Cu kβ
C
O
0
4 KeV
8
12
1 μm
(b)
1 μm
(c)
Cu kα
Fe kα
C
O Ca kα
Fe kβ
Cu kβ
0
KeV
12
100 nm
(d)
1 μm
(e)
100 nm
(f)
0.283 nm
5 nm
(g)
Cu kα
Fe kα
Fe kβ
Cu kβ
C
O
Mg
Ca kα
0
KeV
12

Figure 6

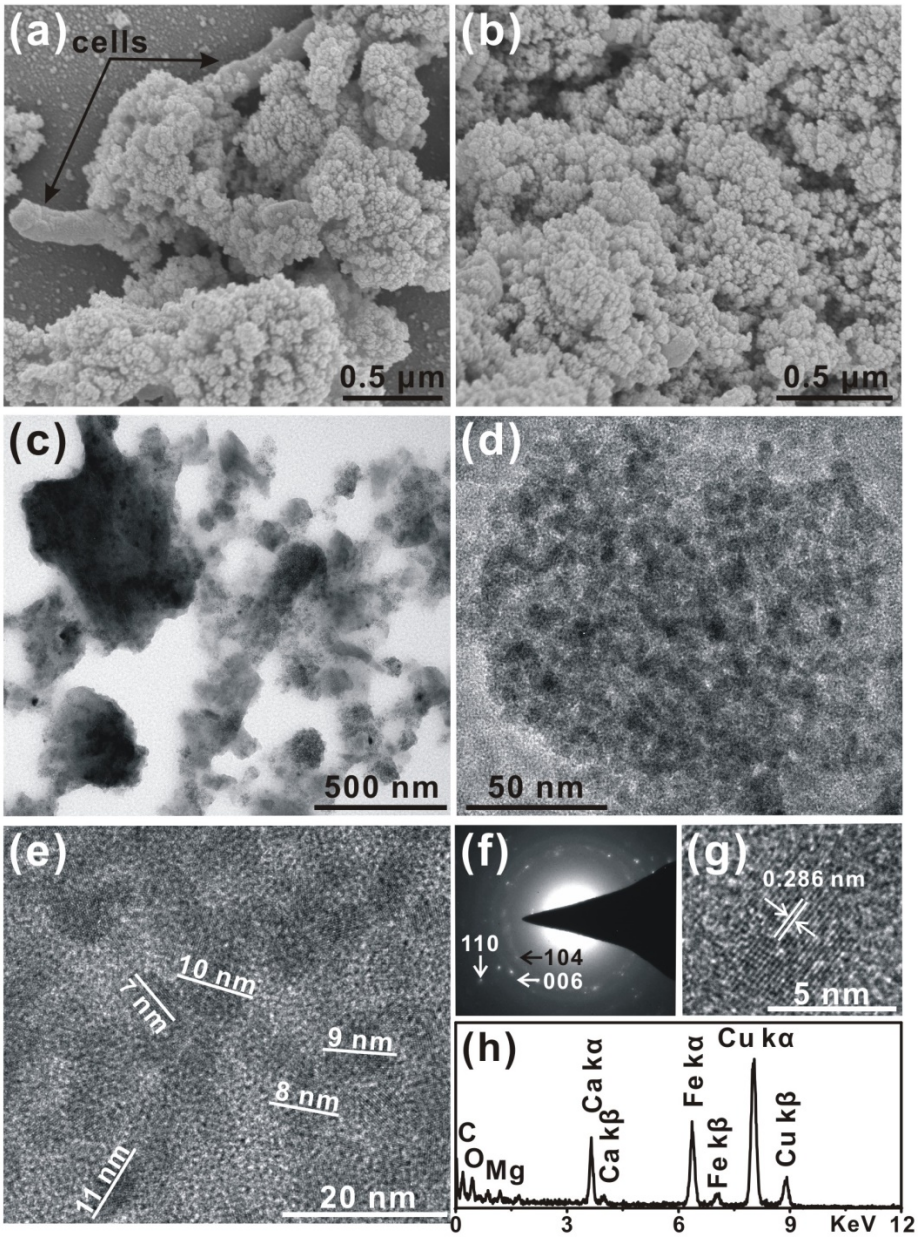
(a)
cells
0.5 μm
(b)
0.5 μm
(c)
500 nm
(d)
50 nm
(e)
10 nm
7 nm
9 nm
8 nm
11 nm
20 nm
(f)
110
104
006
(g)
0.286 nm
5 nm
(h)
C
O
Mg
Ca kβ
Ca kα
Fe kβ
Fe kα
Cu kβ
Cu kα
0
3
6
9
KeV 12

Figure 7

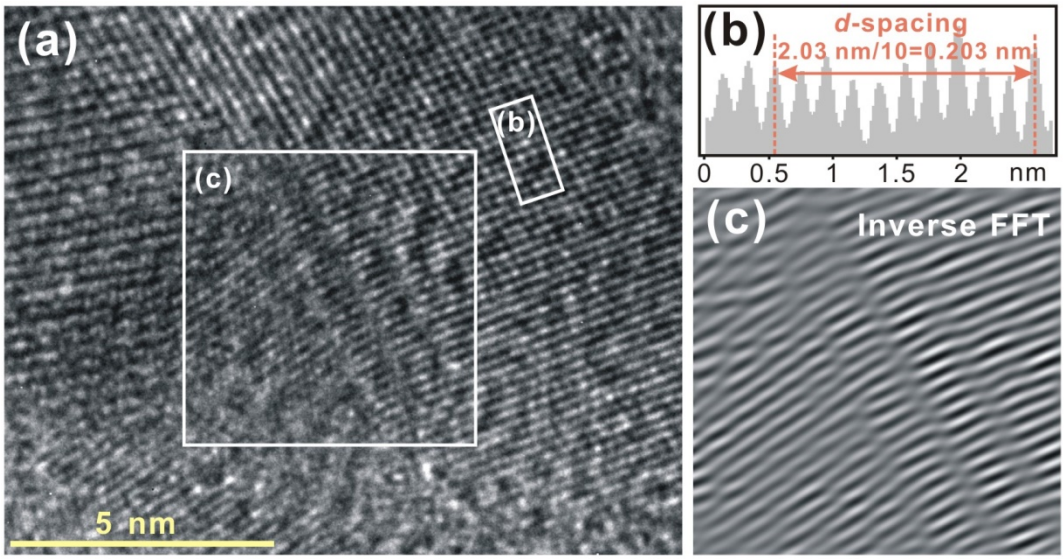

Figure 8

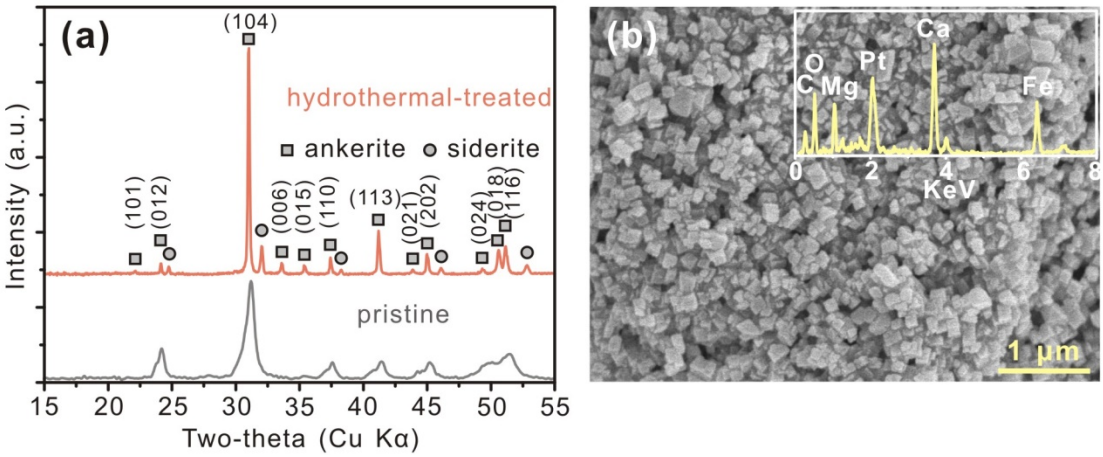
(a)
(104)
hydrothermal-treated
ankerite
siderite
(101)
(012)
(006)
(015)
(110)
(113)
(021)
(202)
(024)
(018)
(116)
pristine
Intensity (a.u.)
15
20
25
30
35
40
45
50
55
Two-theta (Cu Kα)
(b)
O
C
Mg
Pt
Ca
Fe
0
2
4
6
8
KeV
1 μm

Figure 9

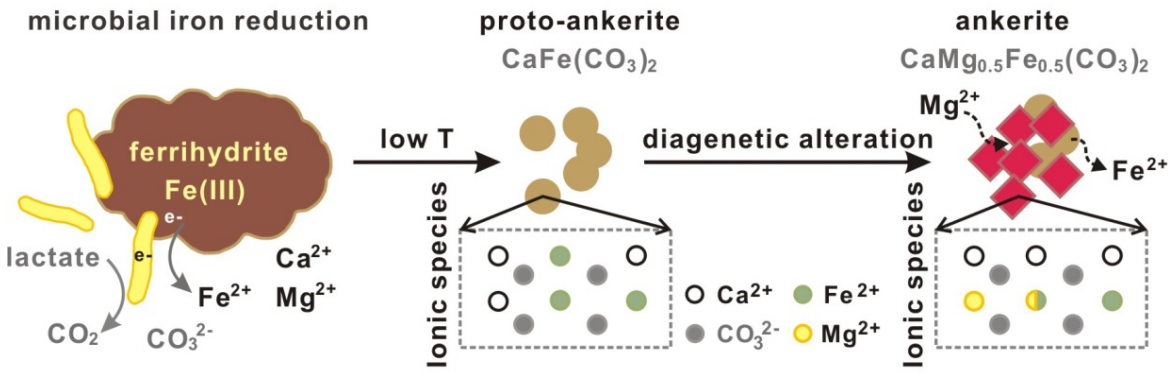
microbial iron reduction
proto-ankerite
CaFe(CO3)2
ankerite
CaMg0.5Fe0.5(CO3)2
ferrihydrite
Fe(III)
e-
e-
lactate
Ca2+
Mg2+
Fe2+
CO2
CO3 2-
low T
diagenetic alteration
Mg2+
Fe2+
Ionic species
Ca2+
Fe2+
CO3 2-
Mg2+
Ionic species

Figure 10